Increasing the structural variety of discrete nondiffracting wave fields

Martin Boguslawski,* Patrick Rose, and Cornelia Denz
Institut für Angewandte Physik and Center for Nonlinear Science (CeNoS), Westfälische Wilhelms-Universität Münster, Corrensstraße 2/4, D-48149 Münster, Germany
(Received 2 March 2011; published 28 July 2011)

We investigate discrete nondiffracting beams (DNBs) being the foundation of periodic and quasiperiodic intensity distributions. Besides the number of interfering plane waves, the phase relation among these waves is decisive to form a particular intensity lattice. In this manner, we systematize different classes of DNBs and present similarities as well as differences. As one prominent instance, we introduce the class of sixfold nondiffracting beams, offering four entirely different transverse intensity distributions: in detail, the hexagonal, kagome, and honeycomb pattern, as well as a hexagonal vortex beam. We further extend our considerations to quasiperiodic structures and show the changeover to Bessel beams. In addition, we introduce a highly flexible implementation of the experimental analog of DNBs, namely discrete pseudo-nondiffracting beams, and present locally resolved intensity and phase measurements, which underline the nondiffracting character of the generated wave fields.

DOI: 10.1103/PhysRevA.84.013832 PACS number(s): 42.40.Jv, 42.30.Kq, 42.25.Hz, 42.79.Hp

I. INTRODUCTION

In recent years, so-called nondiffracting wave fields have become an important and well-researched topic in the fields of optical trapping [1,2] and optical induction of photonic lattices in photosensitive media [3–6], as well as optical atom traps for Bose-Einstein condensates [7,8]. The distinctive feature of nondiffracting wave fields is a transversely modulated intensity distribution combined with a translation-invariant intensity in the direction of propagation [9], which makes an optical generation of largely expanded two-dimensional structures in variable structural sizes highly feasible. In this context, a significant benefit is the self-healing effect, in which a disturbance occurring at a localized area of the nondiffracting wave field is corrected with continuous propagation [10]. Starting in the year 1987 with the prediction and experimental implementation of the Bessel beam [11–13], in the following years the focus was put on the examination of nondiffracting beams characterized by a field distribution in curvilinear symmetries. It was already known that there are four different families of nondiffracting beams, and an extensive investigation was carried out for Bessel beams [14] and Mathieu beams [15,16], as well as Weber beams [17,18]. However, only small efforts were put into characterizing the beam family that is described in Cartesian coordinates, namely discrete nondiffracting beams (DNBs). In contrast to radially decreasing intensities for the three beam families with curvilinear symmetries, discrete nondiffracting beams reveal radially independent intensities, which is an enormous advantage for the induction of largely expanded photonic lattices.

Probably, the most popular wave field with nondiffracting properties is the interference of two monochromatic plane waves propagating under a given angle, which defines the period of the transverse one-dimensional (1D) intensity modulation. This paper puts forward the derivation and classification of more elaborate waves belonging to the family of discrete nondiffracting beams and discusses the connection to Bessel beams. Furthermore, to confirm the successful implementation of experimental translation-invariant light fields, we exemplarily present measurement results of intensity and phase analyses of selected examples, which are in good agreement with the calculated simulations.

II. SOLUTIONS OF THE HELMHOLTZ EQUATION

In general, nondiffracting beams are scalar solutions $\Psi(\mathbf{r})$ of the time-invariant Helmholtz equation,

$$(\nabla^2 + k^2)\Psi(\mathbf{r}) = 0, \tag{1}$$

with $\mathbf{r} = (x, y, z)$ and k representing the norm of the wave vector $\mathbf{k}$. These solutions can be found by separating the equation into a transverse and a longitudinal differential equation. In the following, we place the Cartesian coordinate system in a manner that z describes the direction of propagation, whereas x and y are the transverse coordinates. Then the time-invariant solution of the longitudinal equation for monochromatic light of the wavelength λ is proportional to $\exp(ik_z z)$, in which k_z describes the longitudinal component of the wave vector $\mathbf{k}$ with $|\mathbf{k}| = (k_x^2 + k_y^2 + k_z^2)^{1/2} = 2\pi/\lambda$. Finding special solutions for the transverse differential equation, which explicitly consist of partial waves exhibiting a fixed transverse component $k_t = (k_x^2 + k_y^2)^{1/2}$, the whole set of nondiffracting wave fields is specified. Due to the fixed longitudinal solution independent from the transverse one, as well as the monochromatic character of the relevant wave fields, k_t is determined automatically.

Such solutions can be derived in four different two-dimensional (2D) coordinate systems, namely Cartesian coordinates and polar coordinates, as well as elliptic coordinates and parabolic coordinates, respectively [19,20]. Thereby, the effect of nondiffracting propagation arises from the fixed phase relation between all interfering partial waves. Hence, in Fourier space, the $\mathbf{k}$ vectors of the partial waves lie on the surface of a cone with a defined opening angle θ, which depends on the transverse component k_t, since

$$k_t = |\mathbf{k}| \sin(\theta/2). \tag{2}$$

*martin.boguslawski@uni-muenster.de

 ©2011 American Physical Society

Given that k_t determines the structural size of the grating in real space, a generalized lattice period g can be introduced for the intensity distribution of the wave fields of all nondiffracting beam families by $g = \pi/k_t$.

The DNB family is deeply connected with a periodic and a quasiperiodic transverse intensity distribution, respectively [9]. Thereby, the associated order of rotational symmetry is determined by the amount of interfering plane waves bearing a nondiffracting beam. Thus the superposition of n plane waves leads to a transverse intensity distribution with a rotational symmetry of at least n. In the following, we solely concentrate on those special cases at which the delta distributions of intensity in the far field (which are the Fourier transformations of the n interfering plane waves in real space) form vertices of equilateral n-fold polygons. To increase the structural manifold of DNBs with equal rotational symmetry, we introduce an additional parameter m by varying the phase relation between adjacent beam forming plane waves in Fourier space. Hence the resulting time-dependent complex field distribution $\Psi_{n,m}$ in Cartesian coordinates is specified by

$$\Psi_{n,m}(\mathbf{r},t) = \Psi_0 \sum_{j=1}^{n} \exp\left\{ i\left(k_{x,j}x + k_{y,j}y + k_z z + j\frac{\Phi_m}{n} - \omega t \right)\right\}, \tag{3}$$

with

$$\Phi_m = m\ 2\pi \tag{4}$$

indicating the total initial phase shift between all participating plane waves. Hence, by impressing an absolute phase $j\ \Phi_m/n$ onto the jth plane wave in Fourier space, a fixed phase difference Φ_m/n between adjacent discrete wave components appears. Indeed, the phase parameter m generally describes qualitatively different wave fields compared to the usual case $m = 0$. Thereby, to describe all possible wave fields for a fixed n, it is sufficient to contemplate m in the interval

$$0 \leqslant m \leqslant \frac{n}{2}, \quad m \in \mathbb{R}, \tag{5}$$

by reason of the following considerations. Due to the 2π periodicity of the phase, all structures with m beyond the interval (5) can also be described by a value that is an element of that interval. Negative m values describe structures with a counterrotating phase distribution compared to the $-m$ case, though the associated intensity distributions are equal. Thus, for a phase difference between adjacent plane waves greater than π, for instance $\Phi_m/n = \pi + \varepsilon$, the phase difference can be wrapped back into the interval $[-\pi,\pi]$ by subtracting 2π, which is $\Phi_m/n - 2\pi = (\pi + \varepsilon) - 2\pi = -(\pi - \varepsilon)$. Hence the resulting intensity distribution $|\Psi|^2$ is equal to the structure of $\Phi_m/n = \pi - \varepsilon$.

III. PERIODIC TRANSVERSE INTENSITY MODULATION

Initially, we concentrate on DNBs with a periodic transverse intensity modulation, implementable by superimposing 2, 3, 4, or 6 plane waves.

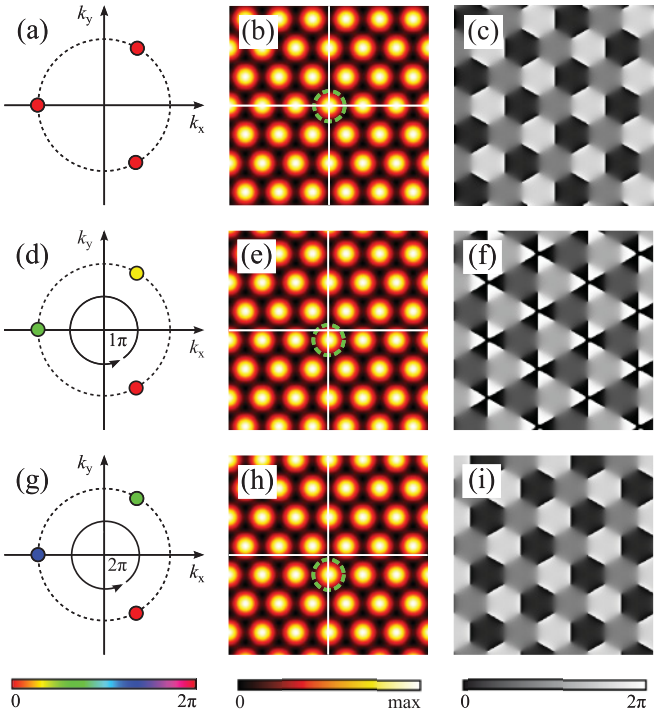

FIG. 1. (Color online) Discrete nondiffracting beam $\Psi_{3,m}$. Left column: illustration of the wave field in Fourier space; closed circles represent plane waves and color maps the relative phase. Middle column: numerical calculation of the transverse intensity distribution. Marked intensity maximum visualizes the traveling of the pattern with varying m. Right column: numerical calculation of the transverse phase distribution. (a)–(c) $m = 0$, (d)–(f) $m = 0.5$, and (g)–(i) $m = 1$.

A. Three interfering plane waves

For the simple and well-known cases of $n = 2,3$, no additional structures besides the 1D modulated intensity and the hexagon structure arise by varying m following Eq. (5). That is, increasing m from 0 to the double of the maximal value of Eq. (5), $m = 2\ n/2 = 3$ for $n = 3$, the invariant intensity pattern travels transversely in one direction, until the initial distribution is reached again due to its periodicity. This behavior, which is well known from the 1D lattice representing the fundament of every interferometry measurement, can also be seen in Fig. 1 for $n = 3$ and $m = 0$ (upper row), $m = 0.5$ (middle row), and $m = 1$ (lower row).

The first column in Fig. 1 illustrates the Fourier plane of the lattice beams with its spatial frequencies. As the frequencies of the contributory beam parts are 2D delta functions, they are depicted as circles in the according as well as in the following diagrams. The color of a circle represents the individual phase. Considering the intensity distribution, the marked lattice sites in Figs. 1(b)–1(h) illustrate the translation of the intensity pattern with varying m, whereupon its direction depends on the particular phase distribution of the plane waves. That is, the general context of a linear phase shift in Fourier space due to a variation of m causing a translation of the pattern in real space can be comprehended here. In contrast to the intensity modulation, the phase pattern of a threefold nondiffracting wave field changes dramatically for a varying m, as becomes definite by comparing Fig. 1(c) with Fig. 1(f), as well as

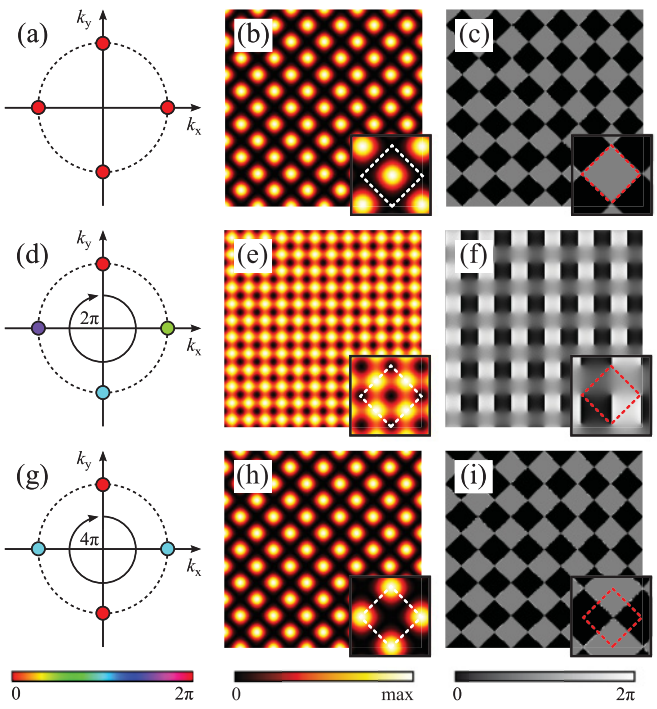

FIG. 2. (Color online) Discrete nondiffracting beam $\Psi_{4,m}$. Left column: illustration of the wave field in Fourier space; closed circles represent plane waves and color maps the relative phase. Middle column: numerical calculation of the transverse intensity distribution. Right column: numerical calculation of the transverse phase distribution. (a)–(c) $m = 0$, (d)–(f) $m = 1$, and (g)–(i) $m = 2$. Magnifications in the lower right corner of every simulation depict the area around the transverse beam center. Dashed rhombs mark a unit cell.

Fig. 1(f) with Fig. 1(i). However, also here, translated similar patterns can be found for different values of m, as a comparison between Figs. 1(c) and 1(i) proves.

B. Four interfering plane waves

As the example of $n = 3$ indicates, an infinite amount of structures can be described by varying m continuously. Nevertheless, in the following, we limit our discussions to the interesting cases of integer values of m. Thus n-fold wave fields bearing vortices of integer topological charge in the transverse center of the beam and occupying distinctive intensity patterns can be regarded. We go on with the description of the transversely fourfold wave field Ψ_{4m}. In doing so, we first consider the cases $m = 0$ and $m = 2$, whose intensity modulation can be identified as the well-known square or diamond pattern. The corresponding intensity and phase distributions are depicted in Figs. 2(b) and 2(h). Such a wave field has been occasionally implemented as a lattice beam to optically induce photonic square or diamond lattices [21,22]. Comparing the $m = 0$ with the $m = 2$ pattern, again a translation of the structure occurs. Also the phase patterns [cf. Figs. 2(c) and 2(i)] only differ by a translation.

However, the intensity distribution for $n = 4, m = 1$, which can be found in Fig. 2(e), is structurally completely different from the former described fourfold case of $m = 0$, bearing a square pattern, although it is fourfold as well. Here, the intensity modulation, which resembles a 45° tilted checkerboard, can be characterized as alternating lines of intensity maxima and minima, whereas the intensity of each line is modulated, additionally. A unit cell of such a structure consists of two intensity maxima and two minima [23,24]. Paying attention to Fig. 2(f), the associated phase distribution bears a completely different structure compared to the $m = 0$ wave field. Thus the $m = 1$ pattern consists of vortices with a topological charge of ± 1, arranged in the typical square alignment. Noteworthy is that sites where vortices are placed correspond to sites of minimum value in the intensity illustration of the wave field. In contrast to that, intensity maxima coincide with areas of homogeneous phase.

C. Six interfering plane waves

Considering Eq. (5), four completely different sixfold structures can be distinguished by interfering six plane waves and varying the value m between integer numbers of 0 and 3. These structures have in common that their unit cells have sixfold symmetry, in contrast to structures that are characterized by noninteger values of m. Figure 3 shows the Fourier space spectrum (left column), as well as the transverse intensity modulation in the middle column containing a magnification of the unit cell of the real space pattern. Further, the phase distribution of each of the four sixfold beam intensities is depicted in the right column.

For $m = 0$, connected to plane waves with equal phase [cf. Fig. 3(a)], the well-known hexagonal structure occurs, which is pictured in Fig. 3(b). An intensity maximum can be found in the center of the beam, which generally coincides with the rotational center of every nondiffracting beam. The corresponding phase distribution consists of areas of equal phase, bordered by circles of π phase shifts as depicted in Fig. 3(c).

Increasing the phase parameter to $m = 1$, the field distribution arises as a composition of nondiffracting vortices arranged in a sixfold manner [25]. Therefore, the corresponding intensity and phase distributions are shown in Figures 3(d)–3(f). In the latter picture, phase singularities with a clockwise increasing phase and hexagonally arranged are prominent. Again, areas of singularities are closely connected with local minima in the intensity picture, each enclosed by honeycomb-like intensity shapes [cf. Fig. 3(e)]. This nondiffracting beam is an interesting case for applications regarding the transfer of angular momentum to particles [26,27].

Besides hexagonal and honeycomb sixfold structures, there exists a third manner to tessellate a 2D area periodically, namely the kagome pattern. Such a structure can be found by determining $m = 2$; thus the complete phase shift between all six beam forming plane waves is $\Phi_2 = 4\pi$. Figures 3(g)–3(i) represent the intensity distribution in Fourier space and in real space, as well as the phase distribution in real space. Vortices of topological charge 1 and 2, visible in the phase pattern of Fig. 3(i), raise intensity minima, which are origins of the typical transverse kagome intensity distribution, consisting of hexagonal and hourglass shapes. Moreover, it is valid, and can be confirmed by Figs. 3(h) and 3(i), that the area of

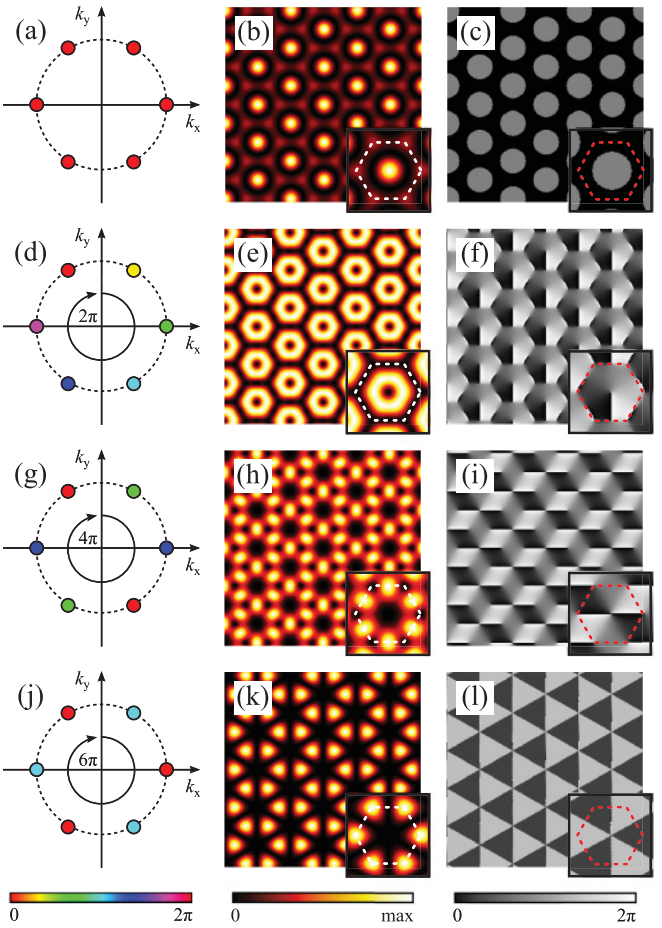

FIG. 3. (Color online) Discrete nondiffracting beam $\Psi_{6,m}$. Left column: illustration of the wave field in Fourier space; closed circles represent plane waves and color maps the relative phase. Middle column: numerical calculation of the transverse intensity distribution. Right column: numerical calculation of the transverse phase distribution. (a)–(c) $m = 0$, (d)–(f) $m = 1$, (g)–(i) $m = 2$, and (j)–(l) $m = 3$. Magnifications in the lower right corner of every simulation depict the area around the transverse beam center. Dashed hexagons mark a unit cell.

low intensity increases with the rising topological charge of a vortex. In general, such lattice beams are predestined to be applied for an optical induction of the exciting kagome pattern in photosensitive media [28], offering new possibilities of linear and nonlinear beam propagation arising from distinct band structures [29].

The fourth alternative to implement a sixfold nondiffracting beam is defining $m = 3$, which puts forth a honeycomb lattice beam, whose corresponding distributions are depicted in Figs. 3(j)–3(l). The transverse intensity pattern of Fig. 3(k) is characterized by graphene-like arranged and triangularly shaped intensity spots. These spots converge with the center of triangles of homogeneous phase in the phase depiction of Fig. 3(l). Again, singularities appear in the phase distribution, in this case at the corners of the triangles containing six π-phase jumps, which affect a region of minimum amplitude noticeable in the intensity distribution. At the edges of every phase triangle appears a π-phase jump as well, which in turn drops the amplitude of the nondiffracting wave field. This nondiffracting wave field can be used as a lattice beam inducing a pattern that reveals stable dipole-mode gap soliton propagation [30].

IV. QUASIPERIODIC TRANSVERSE INTENSITY MODULATION

So far, we exclusively concentrated on nondiffracting beams that show a periodic transverse intensity modulation. It is well known that solely two-, three-, four-, and sixfold patterns reveal a periodic tessellation of a 2D plane, though structures exhibiting a rotational symmetry of $2\pi/n$ with $n = 5,7,8,\ldots$ are characterized as quasiperiodic. Hence Eq. (3) bears solutions with a quasiperiodic phase and intensity distribution for $n = 5,7,8,\ldots$. Again, there is a continuous transition between different intensity patterns for an increasing m, analogous to periodic DNBs. However, field distributions with integer values of m show a rotational center of the structure coinciding with the center of the beam as well. Exemplarily, we describe two wave fields possessing a quasiperiodic transverse intensity modulation: in detail, $n = 5$ offering the famous Penrose pattern [5] and $n = 10$ determining a decagonal transverse intensity pattern [31].

In Figs. 4(a)–4(c), the intensity distributions for $n = 5$ and $m = 0,1,2$ are depicted. Remarkably, the different Penrose patterns for varying integer values of m are nearly similar, only rearrangements of fivefold building blocks constitute the differences to each other. Again, an intensity maximum is placed in the center of the beam for $m = 0$ [cf. Fig. 4(a)]. In contrast to that, intensity minima can be found in the center of the beam for $m \neq 0$, whose area increases with the rising value of $|m|$, which again can be linked to the occurrence of a vortex with topological charge m in Fourier space.

This behavior becomes more significant for wave fields of higher n, such as decagonal intensity distributions with $n = 10$, for instance, as depicted in Figs. 5(a)–5(f). In Fig. 5(a), the center of the beam is similar to the center of a Bessel beam of zeroth order, containing an intensity maximum surrounded by rings of less intensity compared to the center maximum. Both wave fields carry no topological charge, in contrast to the beam given by $m = 1$ [cf. Fig. 5(b)], resembling a Bessel beam of first order. While m is increasing, the area of similarity to the Bessel beam constricts [cf. Fig. 5(c)] and an additional azimuthal modulation of the center surrounding rings becomes prominent [cf. Figs. 5(d) and 5(e)]. Finally, the beam ends up in a wave field whose center is identical to one of a modulated Bessel beam of fifth order [32–34], as illustrated in Fig. 5(f).

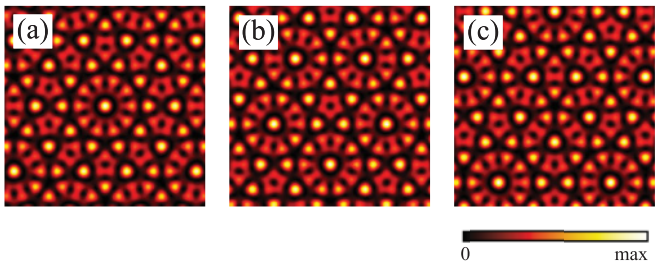

FIG. 4. (Color online) Simulated intensity modulations of $\Psi_{5,m}$ beams for (a) $m = 0$, (b) $m = 1$, and (c) $m = 2$.

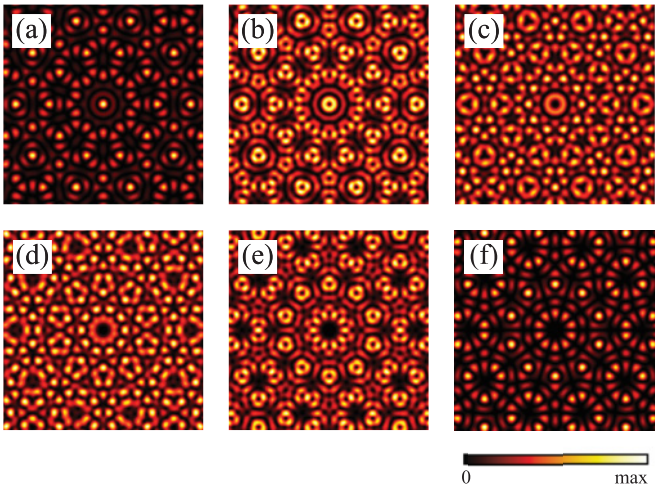

FIG. 5. (Color online) Simulated intensity modulations of a $\Psi_{10,m}$ beam for (a) $m = 0$, (b) $m = 1$, (c) $m = 2$, (d) $m = 3$, (e) $m = 4$, and (f) $m = 5$.

As occasionally mentioned earlier, all discussed wave fields have in common that the center of the $m = 0$ beam exhibits an intensity maximum, in contrast to higher values of m revealing an intensity minimum. The area of the implied minimum becomes larger with increasing m within the bounds of Eq. (5), associated with a local singularity of various topological charge, that can be identified in the phase depiction. A similar behavior can be found in terms of a nondiffracting Bessel beam of the order m. Comparing either, there exists an area of similarity in the center of each beam, as observed for the $\Psi_{10,m}$-wave fields. This area becomes increasingly larger with ascending n. However, with a fixed value of n, an azimuthal intensity modulation progressively supplants the Bessel beam area around the center of the DNB field with rising m, and the transformation of the central area ends up in a field similar to a modulated Bessel beam of the order n for the maximum value of m in terms of Eq. (5). In Fig. 6, the intensity distributions of a DNB with $n = 42$ and varying m as well as of a (modulated) Bessel beam of order m are depicted. It was already shown that DNBs can be implemented by interfering nondiffracting Bessel beams [35], which indicates that nondiffracting beam families are transformable among each other. The described behavior of DNBs implies that also Bessel beams can be developed in the frame of DNBs.

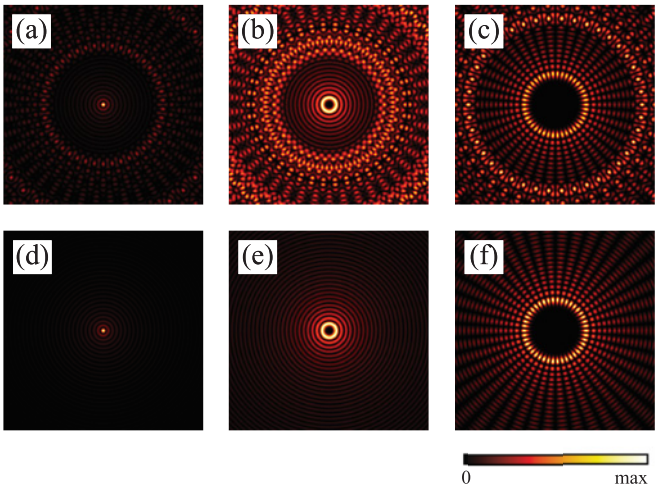

FIG. 6. (Color online) Intensity simulations for $\Psi_{42,m}$ DNBs (first row) and (modulated) Bessel beams of different order (second row). (a) DNB of $n = 42, m = 0$; (b) $m = 4$; (c) $m = 21$; (d) Bessel beam of zeroth order; (e) Bessel beam of fourth order; (f) modulated Bessel beam of 21st order.

V. EXPERIMENTAL IMPLEMENTATION

In general, nondiffracting beams are infinitely expanded in the direction of propagation, carrying infinite energy, which is not achievable in experiments. Further natural confinements are finite apertures of optical elements. Nonetheless, the experimentally implemented analog to nondiffracting beams called pseudo-nondiffracting can be understood as Helmholtz-Gaussian wave fields [36,37], both transversely or longitudinally constrained to a finite volume. Within an area around the transverse beam center, whose diameter certainly depends on the used optical components, Helmholtz-Gaussian wave fields approximately conform to DNBs. In the following, the experimentally implemented wave fields are denoted as discrete pseudo-nondiffracting beams (DPNBs).

Oftentimes, the utilization of a spatial light modulator is suggested to holographically generate arbitrary pseudo-nondiffracting wave fields [38], which convinces by its simple beam alignment. To integrate this technique into a DPNB implementing setup as illustrated in Fig. 7, we expand a frequency-doubled Nd:YAG (yttrium aluminum garnet) laser beam ($\lambda = 532$ nm) to a transversely broad plane wave and send it to the reflective surface of the SLM. The reflected beam experiences a phase retardation according to a phase pattern of the desired nondiffracting beam given to the SLM. In detail, the phase information is calculated directly by determining the argument of the complex-valued field distribution $\Psi_{n,m}$ per $\varphi = \arctan\{\mathrm{Im}(\Psi_{n,m})/\mathrm{Re}(\Psi_{n,m})\}$. A system of mirrors and

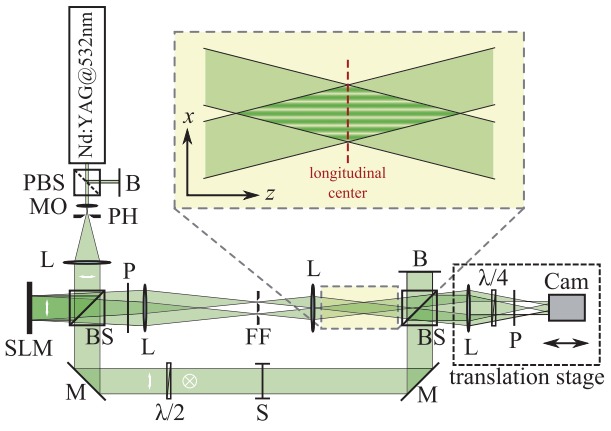

FIG. 7. (Color online) Schematic of the experimental setup. B: light blocker; Cam: camera; FF: Fourier filter; L: lens; M: mirror; MO: microscope objective; P: polarizer; (P)BS: (polarizing) beam splitter; PH: pin hole; S: shutter; SLM: phase-only spatial light modulator. The magnification shows the interference zone of a DPNB, illustrated as a transversely cosine modulated intensity. In here, the dashed line marks the longitudinal center.

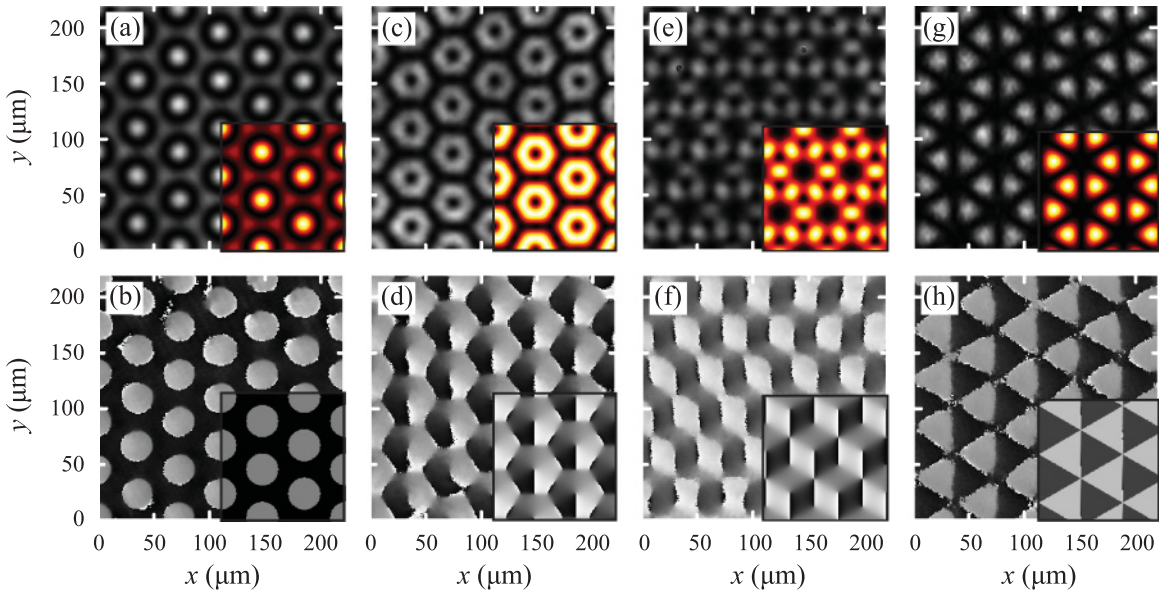

FIG. 8. (Color online) Experimental pictures of transverse intensity (upper row) and phase distribution (lower row) of sixfold beams $\Psi_{6,m}$. Insets show the according simulation. (a),(b) Intensity and phase of the hexagon lattice with $m = 0$; (c),(d) vortex lattice with $m = 1$; (e),(f) kagome lattice with $m = 2$; (g),(h) honeycomb lattice with $m = 3$.

telescopes images the SLM to a particular plane in real space, which is the longitudinal center of the implemented DPNB (cf. magnified inset in Fig. 7). Due to the (quasi)periodicity of the light modulating phase pattern, several diffraction orders are prominent in Fourier space. Therefore, it is necessary to additionally modulate the amplitude of the wave field, which can easily be done in the Fourier plane (indicated as FF in Fig. 7) by blocking all diffraction orders except the first one. Thus a particular intensity filter assures the appropriate propagation of the first diffraction order.

For the analysis of the intensity distributions of the generated wave fields, we employ a camera imaging the intensity in real space. In order to additionally measure the phase of the implemented wave field, we superimpose a reference plane wave and the DPNB. The reference beam holds a fixed phase and an orthogonal polarization compared to the investigated beam, whereby the superposition bears a wave field of arbitrarily elliptical polarization. Consequently, a Stokes parameter measurement to detect the polarization state of a light field extracts the phase connection between the lattice beam and the reference beam, as described in [39]. Hence we are able to depict the locally resolved transverse phase information of an experimentally developed DPNB.

To exemplify the implementation of an arbitrary DPNB, we first concentrate on the analysis of the four different sixfold DPNBs with integer values of m by depicting transverse intensity and phase distributions in Fig. 8. The generated beams have a lattice period of $g = 24\ \mu$m, where the image plane of the camera is identical to the longitudinal center plane of each generated beam. Paying attention to the upper

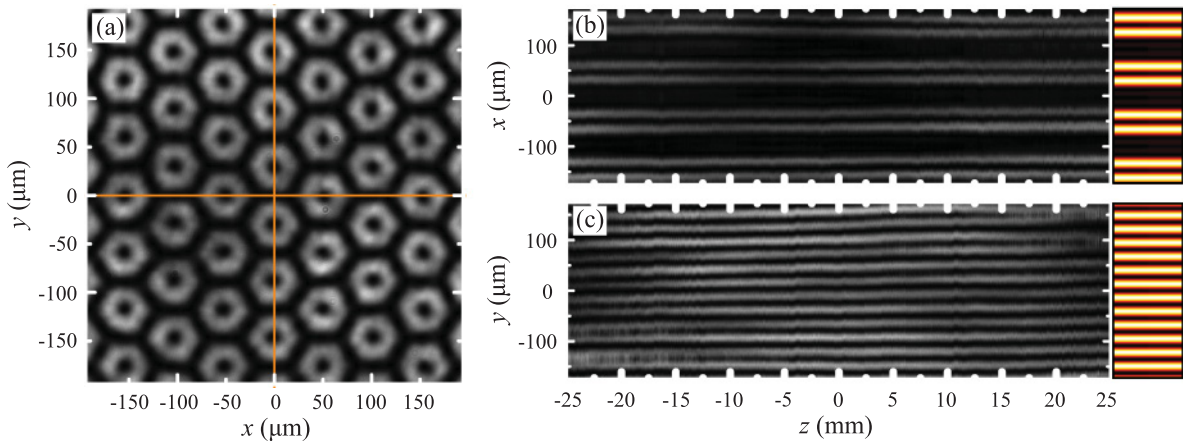

FIG. 9. (Color online) Experimental inspection of the nondiffracting character of a sixfold vortex DPNB $\Psi_{6,2}$. (a) Measured transverse intensity pattern; lines indicate location of planes shown in (b) and (c). Experimentally determined intensity in (b) x-z plane and (c) y-z plane including the rotational center of the beam. Simulations of the intensity development in either plane are illustrated in the boxes beside experimental z-propagation pictures.

row of Fig. 8, it is remarkable to find a huge similarity between the measured and the above introduced simulated intensities, which are accordingly depicted in the lower right quarter of the experimental picture. Thus every characteristic intensity distribution of each implemented sixfold DPNB is definitely identifiable. Besides the intensity distributions, also the measured phase distributions match excellently the simulated patterns, as can be seen in the lower row of Fig. 8, which indicates the experimental implementation of a particular DPNB in one plane.

Additionally, we verify the nondiffracting property of the generated wave field. To facilitate such a measurement, we mount the real space camera as well as an imaging lens onto a translation stage, operating in the direction of the field propagation, denoted as z. The translation stage has an operation range of 10 cm at a resolution of 100 nm. In this manner, we are able to display the longitudinal intensity development of the implemented DPNB in one x-z and y-z plane, respectively. That is, we stack particular rows or columns of pictured intensities for several propagation distances to retrieve the desired information. In Fig. 9, the transverse intensity distribution as well as the intensity development in z direction of a DPNB with $n = 6, m = 1$ is depicted. Again, the transverse lattice period of the beam is fixed to $g = 24\ \mu$m. By reason of the qualitatively matching intensity modulations, a huge conformity between simulation and measurement is prominent, especially around the transverse and longitudinal center of the intensity distribution, declared as 0 μm for transverse dimensions x and y as well as 0 mm for z. The pictures in Figs. 9(b) and 9(c) indicate a longitudinal length of the developed nondiffracting beam of at least 5 cm at a lattice period of $g = 24\ \mu$m. In our measurements, the mean full width at half maximum (FWHM) of one intensity maximum in the vicinity of the transverse beam center and in a z range of -25 mm to 25 mm is $d_{\mathrm{FWHM},x} = (14.40 \pm 0.02)\ \mu$m for the x-z plane and $d_{\mathrm{FWHM},y} = (14.36 \pm 0.02)\ \mu$m for the y-z plane, respectively. In contrast, a Gaussian beam, whose minimum beam waist ω_0 is comparable to $d_{\mathrm{FWHM}}/2$, experiences a broadening of the beam waist at $z = \pm 25$ mm to a diameter of $w(z = \pm 25\ \mathrm{mm}) \approx 590\ \mu$m. The corresponding Rayleigh range of the Gaussian beam is $z_R \approx 0.58$ mm; thus the detected longitudinal nondiffracting range of the investigated light field is approximately 80 times larger than z_R. Our investigation confirms the nondiffracting character of the implemented wave fields as the longitudinal range, in which the intensity stays constant, is several orders of magnitude larger than the Rayleigh range of a Gaussian beam with comparable beam waist.

VI. CONCLUSION

In summary, we have characterized and systematized the family of discrete nondiffracting beams by describing the field distribution with two parameters n and m, whereupon n determines the number of plane waves forming a nondiffracting wave field per superposition and m establishes a constant phase step between each plane wave. The variation of both parameters causes a huge structural diversity of transverse intensity modulations, where the occurrence of the essentially different intensity as well as phase patterns of the four introduced sixfold DNBs has to be pointed out. Besides these periodic lattice beams, wave fields holding quasiperiodic intensity modulations also belong to the discussed beam family. In this context, we pointed out that a nondiffracting wave field with $n \to \infty$ converges to the field distribution of a Bessel beam of particular order. Our experimental results demonstrate the similarities between theoretical DNBs and experimentally implemented DPNBs in terms of the spatial expansion of the latter field, whereby we could confirm exemplarily the generation of any desired wave field by transversely resolved images of the intensity, as well as the phase distribution. Additionally, we could indicate that a sixfold vortex DPNB with a lattice period of tens of micrometers reveals a nondiffracting character over a finite length that is approximately 80 times larger than the Rayleigh range of a comparable Gaussian beam. This behavior is representative for the whole family of discrete nondiffracting beams.

[1] D. Benito, D. Carberry, S. Simpson, G. Gibson, M. Padgett, J. Rarity, M. Miles, and S. Hanna, Opt. Express **16**, 13005 (2008).

[2] C. Alpmann, R. Bowman, M. Woerdemann, M. Padgett, and C. Denz, Opt. Express **18**, 26084 (2010).

[3] V. Berger, O. Gauthier-Lafaye, and E. Costard, J. Appl. Phys. **82**, 60 (1997).

[4] J. W. Fleischer, T. Carmon, M. Segev, N. K. Efremidis, and D. N. Christodoulides, Phys. Rev. Lett. **90**, 023902 (2003).

[5] J. W. Fleischer, G. Bartal, O. Cohen, T. Schwartz, O. Manela, B. Freedman, M. Segev, H. Buljan, and N. Efremidis, Opt. Express **13**, 1780 (2005).

[6] B. Freedman, G. Bartal, M. Segev, R. Lifshitz, D. N. Christodoulides, and J. W. Fleischer, Nature (London) **440**, 1166 (2006).

[7] L.-M. Duan, E. Demler, and M. D. Lukin, Phys. Rev. Lett. **91**, 090402 (2003).

[8] B. Damski, H. Fehrmann, H.-U. Everts, M. Baranov, L. Santos, and M. Lewenstein, Phys. Rev. A **72**, 053612 (2005).

[9] Z. Bouchal, Czech. J. Phys. **53**, 537 (2003).

[10] Z. Bouchal, J. Wagner, and M. Chlup, Opt. Commun. **151**, 207 (1998).

[11] J. Durnin, J. J. Miceli Jr., and J. H. Eberly, Phys. Rev. Lett. **58**, 1499 (1987).

[12] J. Durnin, J. Opt. Soc. Am. A **4**, 651 (1987).

[13] F. Gori, G. Guattari, and C. Padovani, Opt. Commun. **64**, 491 (1987).

[14] C. A. McQueen, J. Arlt, and K. Dholakia, Am. J. Phys. **67**, 912 (1999).

[15] J. C. Gutiérrez-Vega, M. D. Iturbe-Castillo, and S. Chávez-Cerda, Opt. Lett. **25**, 1493 (2000).

[16] J. C. Gutiérrez-Vega, M. D. Iturbe-Castillo, G. A. Ramírez, E. Tepichín, R. M. Rodríguez-Dagnino, S. Chávez-Cerda, and G. H. C. New, Opt. Commun. **195**, 35 (2001).

[17] M. A. Bandres, J. C. Gutiérrez-Vega, and S. Chávez-Cerda, Opt. Lett. **29**, 44 (2004).
[18] B. M. Rodríguez-Lara, J. Opt. Soc. Am. A **27**, 327 (2010).
[19] E. G. Kalnins and W. Miller, J. Math. Phys. **17**, 331 (1976).
[20] W. Miller Jr., *Symmetry and Separation of Variables*, Encyclopedia of Mathematics and its Applications Vol. 4 (Addison-Wesley, Reading, MA, 1977).
[21] A. S. Desyatnikov, N. Sagemerten, R. Fischer, B. Terhalle, D. Träger, D. N. Neshev, A. Dreischuh, C. Denz, W. Krolikowski, and Y. S. Kivshar, Opt. Express **14**, 2851 (2006).
[22] B. Terhalle, A. S. Desyatnikov, C. Bersch, D. Träger, L. Tang, J. Imbrock, Y. S. Kivshar, and C. Denz, Appl. Phys. B **86**, 399 (2007).
[23] P. Zhang, S. Liu, C. Lou, F. Xiao, X. Wang, J. Zhao, J. Xu, and Z. Chen, Phys. Rev. A **81**, 041801 (2010).
[24] J. Yang, P. Zhang, M. Yoshihara, Y. Hu, and Z. Chen, Opt. Lett. **36**, 772 (2011).
[25] J. Becker, P. Rose, M. Boguslawski, and C. Denz, Opt. Express **19**, 9848 (2011).
[26] H. He, M. E. J. Friese, N. R. Heckenberg, and H. Rubinsztein-Dunlop, Phys. Rev. Lett. **75**, 826 (1995).
[27] Z. Bouchal, J. Opt. Soc. Am. A **21**, 1694 (2004).
[28] M. Boguslawski, P. Rose, and C. Denz, Appl. Phys. Lett. **98**, 061111 (2011).
[29] K. J. H. Law, A. Saxena, P. G. Kevrekidis, and A. R. Bishop, Phys. Rev. A **79**, 053818 (2009).
[30] P. Rose, T. Richter, B. Terhalle, J. Imbrock, F. Kaiser, and C. Denz, Appl. Phys. B **89**, 521 (2007).
[31] K. J. H. Law, A. Saxena, P. G. Kevrekidis, and A. R. Bishop, Phys. Rev. A **82**, 035802 (2010).
[32] Y. V. Kartashov, A. A. Egorov, V. A. Vysloukh, and L. Torner, Phys. Rev. E **70**, 065602(R) (2004).
[33] R. Fischer, D. N. Neshev, S. López-Aguayo, A. S. Desyatnikov, A. A. Sukhorukov, W. Krolikowski, and Y. S. Kivshar, J. Mater. Sci.: Mater. Electron. **18**, S277 (2007).
[34] S. Xu, J. Liang, and L. Yi, J. Opt. Soc. Am. B **27**, 99 (2010).
[35] V. Arrizón, S. Chávez-Cerda, U. Ruiz, and R. Carrada, Opt. Express **15**, 16748 (2007).
[36] J. C. Gutiérrez-Vega and M. A. Bandres, J. Opt. Soc. Am. A **22**, 289 (2005).
[37] Z. Bouchal, Czech. J. Phys. **55**, 1223 (2005).
[38] N. Chattrapiban, E. A. Rogers, D. Cofield, W. T. Hill III, and R. Roy, Opt. Lett. **28**, 2183 (2003).
[39] V. G. Denisenko, A. Minovich, A. S. Desyatnikov, W. Krolikowski, M. S. Soskin, and Y. S. Kivshar, Opt. Lett. **33**, 89 (2008).